Progress In Electromagnetics Research, Vol. 118, 355–377, 2011

FIELD SYNTHESIS IN INHOMOGENEOUS MEDIA: JOINT CONTROL OF POLARIZATION, UNIFORMITY AND SAR IN MRI B_1-FIELD

E. A. Attardo[1,*], T. Isernia[2], and G. Vecchi[1]

[1]Dipartimento di Elettronica, Politecnico di Torino, Turin, Corso Duca Degli Abruzzi 24, 10129, Italy

[2]Dipartimento di Informatica, Matematica, Elettronica e Trasporti (DIMET) Universita degli Studi Mediterranea di Reggio Calabria, Via Graziella, Loc. Feo di Vito, Reggio Calabria 89100, Italy

Abstract—The homogeneity of the amplitude of one of the polarizations of the RF field $\underline{B}_1$ is a crucial issue in Magnetic Resonance Imaging (MRI), and several methods have been proposed for enhancing this uniformity ("Shimming"). The existing approaches aim at controlling the homogeneity of B_1^+ and limiting the Specific Absorption Rate (SAR) of the RF field by independently controlling magnitude and phase of individual excitation currents in MRI scanners, either birdcage or TEM coil system. A novel approach is presented here which allows a joint control of B_1^+ uniformity, SAR, and purity of polarization of the total RF $\underline{B}_1$ field. We propose a convex optimization procedure with convex constraints, and special attention has been devoted to the issue of convexity of the proposed functional. The method is applied to MRI brain imaging; numerical tests have been performed on a realistic head model at low, medium, and high RF field in order to assess the effectiveness of the proposed method. We found that maintaining a specific polarization plays an important role also in maintaining the homogeneity of B_1^+ amplitude.

1. INTRODUCTION

One of the most critical factor that influence the quality and resolution of Magnetic Resonance Imaging (MRI) is the homogeneity of the amplitude of one of the polarizations of the RF field $\underline{B}_1$. Because of the non homogeneity of the scenario, and of the intrinsic difficulty

Received 19 May 2011, Accepted 14 June 2011, Scheduled 7 July 2011

* Corresponding author: Elia Amedeo Attardo (elia.a.attardo@dartmouth.edu).

of such a constraint, the field usually obtained is far from the one required. This is especially the case for recent high and ultra-high field ($B_0 \geq 7\,\mathrm{T}$), with the consequent increase of the frequency of the RF field. As a result, the issue of leveling ("shimming") the B_1^+ field has received considerable attention in the recent literature [1–3]. In [1] the homogeneity for the RF B_1^+-field is achieved optimizing separately three different quantities, but the problem related to the energy absorption is not addressed. Because of the practical importance of limiting the Specific Absorption Rate (SAR) in both partial and whole body imaging, recent works have addressed the combined task of optimizing RF magnetic field amplitude uniformity while limiting the SAR [2, 3]. Also, in the different contributions, [1–3] discussion on local/global convergence properties of the adopted optimization methods is apparently lacking, leading to optimization procedures, which, as discussed in the following, are subject to possible trapping into sub-optimal solutions.

In the following, a synthesis procedure is proposed for the $\underline{B}_1$ field able to take contemporaneously into account all constraints regarding polarization, homogeneity and strength of the $\underline{B}_1$ field (see below), while being as robust as possible with respect to the possible occurrence of sub-optimal solutions, (i.e., solutions not corresponding to the globally optimal solution of the problem). In fact, by using the real and imaginary parts of the complex excitation currents of the coil (instead of amplitude and phase as in previous approaches), as well as by a suitable formulation of the problem, we are able to reduce the overall problem to a kind of Convex Programming problem. As a consequence, no trapping into sub-optimal solutions is possible, so that the globally optimal $\underline{B}_1$ field, which is of course the real goal, can be achieved in a computationally easy fashion, as well as with a reduced computational burden.

To the best of the authors' knowledge, none of the literature works addresses control of the purity of *polarization* of the $\underline{B}_1$ RF field although [4] explicitly mentions the loss of polarization purity inside the region of interest (ROI) as one of the responsible causes for the loss of homogeneity of the RF field. In this manuscript we will show how an explicit control of polarization purity of the total $\underline{B}_1$-field is needed to maintain the homogeneity of the selected component B_1^+. Many authors have introduced the $\underline{B}_1$ shimming in terms of B_1^+ homogeneity and SAR reduction [1–3] but in these works no control in polarization changing is taken into account. Indeed, quality of MRI anatomical imaging depends on the intensity and homogeneity of B_1^+ field, but also on polarization: degradation of field polarization from the desired circular left-hand to elliptical up to linear polarization is the

cause of higher power emission from the coils, and/or reduced signal-to-noise ratio (SNR) [5]. In turn, even if polarization were optimized in an empty birdcage coil, the presence of biological tissues inside the birdcage introduces permittivity and conductivity non-uniformities that alter field amplitude and polarization.

We show that controlling the ripple of the RF field amplitude (i.e., amplitude-only homogeneity) is not enough to control the polarization. The proposed method aims at controlling field intensity while keeping under control the homogeneity and polarization of the RF magnetic field $\underline{B}_1$, and enforcing a limitation of SAR; the method is devised to operate in a non-homogeneous material scenario, and it is applied to brain imaging. In particular, the reported examples show ability to comply with constraints on SAR and B_1^+ intensity as enforced by FDA [6] or recommended by [7].

As our tests show, the method provides good results not only at low (B_0) field levels, but also for very-high fields ($B_0 \geq 7\,\mathrm{T}$) where spatial variation of electric parameters has the largest influence on B_1^+ quality.

The proposed optimization method to constrained field shimming is described in Section 2; the anatomical models employed in the tests are presented in Section 3.1, and Section 3.2 describes the metrics employed to evaluate the fulfilling of the enforced constraints and the quality of the shimming.

2. JOINT OPTIMIZATION METHOD

As usual in the relevant literature we assume that the electric and geometric nature of the biological tissues in the region of interests is known, and our objective will be to find the (complex) current excitations, $[I_1,\ I_2, \ldots, I_{Nsrc}]$, assigned to the N_{src} conductors in the birdcage structure that produce the $\underline{B}_1$ field. The electric and the magnetic fields produced by a unit current in the nth conductor are indicated by $\underline{e}_n$ and $\underline{b}_n$; knowledge of these fields requires the solution of the EM problem in the Region of Interest (ROI), that can be done by any EM solver (including those commercially available). Obviously, when dealing with a 3D field optimization problem one needs a 3D solver, while a 2D solver is enough for a 2D optimization; conversely, the presented optimization method is entirely independent from the dimensionality of the problem to evaluate the unit responses $\underline{e}_n$ and $\underline{b}_n$. Consequently, we denote the collection of the N_{src} current excitation

coefficients in a column vector $[I]$, and the overall fields as:

$$\underline{B}_1(\underline{r};[I]) = \sum_{n=1}^{N_{src}} I_n \underline{b}_n(\underline{r}) \tag{1}$$

$$\underline{E}(\underline{r};[I]) = \sum_{n=1}^{N_{src}} I_n \underline{e}_n(\underline{r}) \tag{2}$$

These two fields represent the magnetic induction and electric fields, respectively, resulting from a particular choice of the excitation coefficients $[I]$. Our joint optimization problem can be summarized as follows: find the excitation coefficient distribution $[I]$ that

(i) minimizes deviation from uniform amplitude of a selected circularly polarization of the $\underline{B}_1$ field (e.g., circular right-hand (RH));

subject to the constraints that:

(ii) The SAR is bounded everywhere by a given specific value (typically dictated by FDA or ICNIRP);

(iii) The polarization of the field remains close enough to the desired circular RH to guarantee given performances;

(iv) Amplitude of the desired polarization of $\underline{B}_1$ is above a specific target value;

Before we translate the above requirements into specific inequalities, some comments are useful to shed light onto the rationales behind them, which in turn impact on the formulation and solution of the resulting optimization problem. The requirement in (i) is the field *amplitude* homogeneity customarily addressed in the literature (e.g., [1]); it enforces a spatially uniform energy B_1^+ density, which has the positive impact on imaging quality that is well described in the literature, and needs no further comment here. Constraint (ii) is intended to protect the patient against excessive heating (not only in the skin) and to comply with existing regulations and/or recommendations against possible adverse effects of exposure to RF fields; this issue also has been already considered in the literature [8] and needs no further comment. Polarization constraint (iii) is within the main part of the novelties proposed in this work, and its motivations have already been described in Section 1, also with reference to the literature; hence, we observe that this requirement, taken together with SAR limitation (iii) has the system-level meaning of guaranteeing a prescribed SNR performance within the allowed absorption of electromagnetic power.

Finally, the necessity of the requirement (iv) that field amplitude be above a given minimum value is probably less easy to understand; it is however crucial for a meaningful solution. It can indeed be verified that without this requirement B_1^+-field uniformity is often achieved at the expenses of $\underline{B}_1$ field strength; this is, for instance, the case when using an unconstrained linear optimization (also known as inverse-source).

We now proceed to mathematically formulate our constrained optimization problem; in the following, special care will be taken in formulating the constraint inequalities; indeed, we will show that our approach leads to fully convex constraints which will be key in addressing the optimization problem. As far as the polarization behavior is concerned, taking the static magnetic field ($\vec{B}_0$) is along the z direction, breakdown of the $\underline{B}_1$ field into left-hand (LH) and right-hand (RH) circular polarizations is expressed as:

$$\underline{B}_1(\underline{r}) = B_1^-(\underline{r})\hat{p}_1^- + B_1^+(\underline{r})\hat{p}_1^+ \tag{3}$$

where the polarization complex unit vectors are:

$$\hat{p}_1^- = \frac{(\hat{x} - j\hat{y})}{\sqrt{2}} \tag{4}$$

$$\hat{p}_1+ = \frac{(\hat{x} + j\hat{y})}{\sqrt{2}} \tag{5}$$

and where the (complex) amplitudes of the circular polarization are expressed as:

$$B_1^-(\underline{r}) = \hat{p}_1^{-^*} \cdot \underline{B}_1(\underline{r}) = \frac{1}{\sqrt{2}}[B_{1x}(\underline{r}) + jB_{1y}(\underline{r})] \tag{6}$$

$$B_1^+(\underline{r}) = \hat{p}_1^{+^*} \cdot \underline{B}_1(\underline{r}) = \frac{1}{\sqrt{2}}[B_{1x}(\underline{r}) - jB_{1y}(\underline{r})] \tag{7}$$

With the above notation, the optimization endeavor can be formulated as follows:
find the excitations $[I]$ that yields minimum field deviation from a constant value, i.e.,

$$[I] = \arg\min F_2([I]), \quad F_2([I]) \equiv \left\| |B_1^+(\underline{r};[I])|^2 - |B_1^+(\underline{r}_0;[I])|^2 \right\|^2 \tag{8}$$

where $\underline{r}_0$ is a reference point (e.g., center) of the ROI, subject to:

$$SAR(\underline{r}) \leq UBS(\underline{r}) \tag{9}$$

$$|B_1^-(\underline{r})|^2 \leq UBP(\underline{r}) \cdot |B_1^+(\underline{r})|^2 \tag{10}$$

$$B_1^+(\underline{r}_0) \geq B_{1_{desired}}^+ \tag{11}$$

$$SAR(\underline{r}) = \frac{\sigma|\underline{E}(\underline{r})|^2}{2\rho} \tag{12}$$

with σ (S/m) being the conductivity and ρ is the mass density (kg/m^3) of the tissue, UBS and UBP being assigned limiting value profiles, and $B_{1_{desired}}^{+}$ a prescribed minimum field intensity.

The above have the following motivations and meaning:

- Equation (8) enforces a B_1^+-field *amplitude* as homogeneous as possible; note that by dealing with magnitudes of complex fields, the above is different from requiring a constant (complex) field altogether, i.e., spatial phase variations are allowed here. Combining the advantage of a stronger physical meaning and of the resulting better form of the cost functional, power densities (i.e., amplitude squared) were considered here rather than simply the absolute values of the complex fields; in fact, this choice leads to a fourth-order polynomial in F_2, with regularity properties further discussed in the paragraphs below, that lead to improved properties of the overall optimization instance;
- Equation (9) enforces limitations on the SAR in any given point of ROI. We observe that the locus defined by the equality sing in (9) is an hypercylinder, which amounts to saying that constraints (9) are convex in terms of the real and imaginary parts of the unknown coefficients (see [9] for more details);
- Equation (10) is meant to enforce the desired polarization. In fact, provided the cost functional is sufficiently small, $|B_1^+(\underline{r}_0)|$ is almost equal to $|B_1^+(\underline{r})|$, so that enforcing (10) means essentially to keep the undesired polarization under a given threshold, namely:

$$|B_1^-(\underline{r})|^2 \leq UBP(\underline{r}) \cdot |B_1^+(\underline{r}_0)|^2 \tag{13}$$

- Equation (11), provided the cost functional F_2 in (8) is sufficiently small, states that the field is (everywhere) sufficiently intense. Note the reference phase, which can obviously be chosen at one's will, has been fixed herein in such a way that the B_1^+ field is real and positive at the reference point $\underline{r}_0$. Such a circumstance, together with the choice of charging on the cost functional part of the job, allows to deal again with a convex constraint. In fact, the joint consideration of (8) and (11) will induce a field intensity everywhere higher than (or of the same order of) the desired B_1^+, and the constraint comes out to be linear (and hence convex) in terms of the unknowns.

As a consequence of the given choice for the unknowns, all constraints (9)–(11), (13) are convex, so that, as the intersection of convex sets is still convex, the cost functional (8) has to be minimized onto a convex set. It is interesting to note that this would not be the case by using as unknowns amplitude and phase

of the current excitations (as in [1]) In fact, a set which is convex in terms of real and imaginary parts (for instance, a segment in the complex plane) becomes non-convex when observed in a amplitude-phase plane. Then, the proposed formulation, as compared with previous ones, has the advantage of dealing with convex (rather than with generic) constraints. On the basis of the relatively low number of control degrees of freedom (the N_{src} currents), utilization of a global optimization procedure may be reasonable if the quantization of the current amplitudes and phases is limited. Such a global optimization would overcome the occurrence of a possible local minima which would result in a sub-optimal solution of the problem. On the other hand, other useful theoretical results come into play which further simplify the solution of the problem, and justify a convex (deterministic) optimization. In fact, functionals of this kind have been extensively studied in the framework of the solution of quadratic inverse problems including array antenna synthesis [10] and phase retrieval [11], showing that fourth-order polynomial functionals of this kind can be assumed to be convex whenever the number of unknowns is much less than the number of (independent) contributions to the cost functional.

Then, when the requirement that the field intensity is uniform is enforced at a sufficiently fine grid of points, the number of independent quadratic equations which are generated (and hence the number of independent contributions to the cost functional) is much higher than the number of unknowns (which is very limited in the selected application and it is dictated by the number of conductors of the birdcage or number of microstrips in TEM coil). As a consequence, by virtue of the choices which have been made in choosing the cost functional, one can assume that also the cost functional is a convex one, so that the overall problem is reduced to a Convex Programming (CP) one. Therefore, any local optimization procedure will be able to get the globally optimal solution to the problem at hand. To get the maximum reliability of such a conclusion, such a result (based on [10, 11]) has also been successfully checked by comparing results of the proposed Convex Programming Approach to Shimming (COPAS), (which does not require global optimizations), with the ones resulting from a global optimization procedures based on genetic algorithm (GA). In Section 4.2 we will verify the convexity under given constraints. Finally, we observe that alternative formulations using an uniform norm in the cost functional could be used — at the cost of missing the polynomial nature of the cost functional — for example substituting F_2 in (8) with:

$$F_1([I]) = \left\| |B_1^+(\underline{r};[I])| - |B_1^+(\underline{r}_0;[I])| \right\|^2 \tag{14}$$

It is worth to note that the intrinsic limitation of these kinds of methods is in the regularity of the cost function: the functional must have a continuous first derivative (at least) when a gradient-based optimization technique is employed. Therefore, in the following we use formulation (8) and a gradient-based optimization procedure, in particular a Quasi Newton Line Search routine [12].

3. APPLICATION TO MRI

We will now describe one study case used in the following to test the optimization procedure, and the system-level relevant quality indicators to be used to monitor the optimization performances.

The test scenario is a realistic model of the brain. The rationale for using a realistic model of the brain is almost self-evident, since shimming the B_1^+ field is challenging in the presence of a very inhomogeneous media, and all the more so at higher frequencies.

3.1. 2D Realistic Phantom

In this section, we describe the realistic model used. We start with a 3-D grey scale MRI generated by [13]. Each MRI image has been produced taking into consideration a repetition time, τ, equal to 20 ms, and a T_1 scanning modality with a thickness, along the z direction, equal to 1 mm. Also, we consider the simplest pulse sequence known as partial saturation [8]. The images are obtained using a simulator [13]. Once we have the MRI in grey scale we need to obtain a segmented version of the different brain's anatomical structures. According to [13, 14], the digital MRI is classified by different constitutive parts of the brain, which include: cerebrospinal fluid (CSF), grey matter (GM), white matter (WM), fat, muscle, skin, skull, vessels, dura mater (DM) and bone marrow. The segmentations of the single regions are obtained by using [14]. In that model each anatomical tissue is classified using a set of 3-dimensional "fuzzy" membership volumes, one for each class listed above. The voxel value in these volumes reflects the proportion of that tissue type, present in that voxel, in the range $[0, 1]$. The segmentation yields a particular label for different anatomical structures as indicated in Table 1.

Figure 1 depicts the whole assembled head model obtained with the aforementioned procedure. Also, Figure 2 shows the different constitutive parts of the brain.

Different $\underline{B}_0$ field strengths are accounted for by Larmor's frequencies, which are the frequencies of RF B_1^+ field. In order to meaningfully correlate the different RF frequency scenarios, it

Table 1. Labels associated with each anatomical structure.

Label	Name
0	Background
1	CSF
2	Grey Matter
3	White Matter
4	Fat
5	Muscle
6	Skin
8	Vessels
9	Around Fat
10	Dura mater
11	Bone marrow

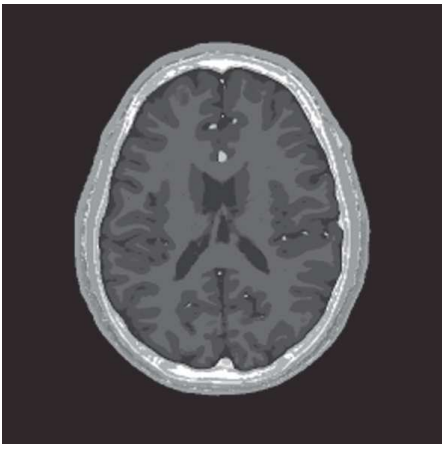

Figure 1. Simulated MRI.

is necessary to account for dispersion [15–17] for each tissues in Table 1. Table 2 shows the selected frequencies with related strength of the static magnetic field $\underline{B}_0$. Tables 3 and 4 represent the relative permittivity and conductivity at each frequency in Table 2, respectively.

We note that mass density values for the tissues above are also necessary to evaluate the SAR, which have been taken from [8].

The realistic model is now obtained by assembling all the different tissues derived from the segmentation operation. Figure 3 shows the dielectric properties at $B_0 = 7\,\mathrm{T}$ and $B_1^+ = f_3$.

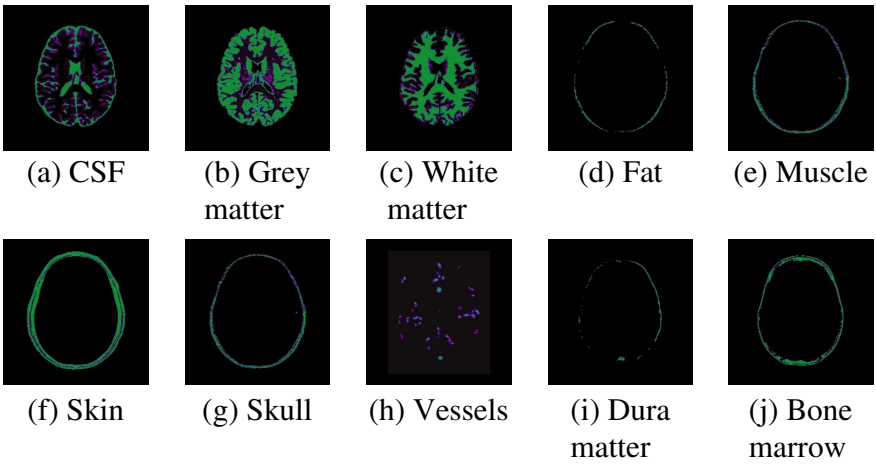

Figure 2. Brain's anatomical structures.

Table 2. Larmor's frequency associated with the static field B_0.

Frequency label	B_0 (T)	B_1^+ (MHz)
f_1	1.5	64
f_2	3	128
f_3	7	300
f_4	9	384
f_5	11	469

Table 3. Relative permittivity for the selected frequencies.

Tissue	f_1	f_2	f_3	f_4	f_5
CSF	97.31	84.04	72.73	71.2	70.32
grey matter	97.43	73.52	60.02	57.76	56.26
White matter	67.84	52.53	43.78	42.29	41.29
Fat	65.06	59.21	56.34	55.87	55.54
Muscle	72.23	63.49	58.2	57.27	56.63
Skin	76.72	61.59	51.9	50.15	48.97
Skull	16.68	14.72	13.44	13.19	13
Vessels	68.64	55.99	48.32	47.17	46.43
Dura mater	73.26	55.97	47.96	46.83	46.11
Bone marrow	72.1	62.33	57.58	56.84	56.34

Table 4. Conductivity for the selected frequencies (Sm^{-1}).

Tissue	f_1	f_2	f_3	f_4	f_5
CSF	2.066	2.143	2.224	2.247	2.269
Grey matter	0.5109	0.5867	0.6924	0.7306	0.7664
White matter	0.2915	0.3421	0.4133	0.4398	0.4649
Fat	0.03527	0.03687	0.03957	0.04086	0.04226
Muscle	0.6882	0.7192	0.7705	0.7922	0.8142
Skin	0.488	0.5442	0.6308	0.6631	0.6936
Skull	0.05953	0.06735	0.08266	0.08992	0.09758
Vessels	0.4293	0.4789	0.537	0.5576	0.578
Dura mater	0.7067	0.7517	0.8036	0.8235	0.8436
Bone marrow	0.02109	0.02363	0.02737	0.0289	0.0306

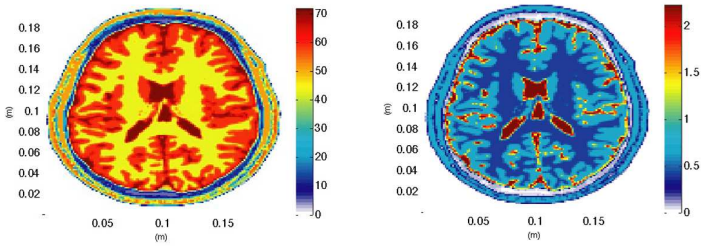

(a) Relative permittivity (b) Conductivity Sm^{-1}

Figure 3. Dielectric properties at $f_3 = 300\,\text{MHz}$.

Additionally, inserting the dielectric properties for each segmented structure depicted in Figure 2 will depend on the employed EM forward solver. As we will briefly describe in Section 4 using a Method of Moments (MoM) with piece-wise constant basis function will allow us to associate each pixel of the image with a specific dielectric constant (conductivity and relative permittivity). Some MATLAB functions have been written to interpolate the dielectric values in order to satisfy the forward solver mesh grid.

3.2. Quality Indicator Parameters

In order to evaluate the results at a system-level, we discuss now the parameters to be used to evaluate the effectiveness of the proposed optimization method, called in the following quality indicators (QI). Such parameters will take into account the shimming of the field as

well as the polarization, the ripple and the flip-angle. In fact, in order to achieve the angular deflection of the magnetic field B_0, it should be possible to produce a B_1^+ field that actually rotates the net magnetization vector, $\underline{M}$. Concerning our setup, B_1^+ should rotate the B_0 in x-y plane, when the B_0 field is z-oriented and when the partial saturation sequence is considered. The ability of the RF field to effectively rotate the B_0 field is a crucial parameter. This parameter is known as a flip-angle. In fact, according to [18], the flip-angle is defined as the degree of rotation of the macroscopic magnetization vector produced by a radio frequency pulse with respect to the direction of the static magnetic field, and is expressed by:

$$\alpha(\underline{r}) = \frac{\gamma\tau}{\mu_0}\left|B_1^+(\underline{r})\right| \tag{15}$$

where γ is the gyromagnetic ratio and τ is the application time of the RF. In partial saturation sequences, a flip-angle $\alpha = \pi/2$ is required inside ROI in order to have the complete deflection of the static field in the x-y plane. It is apparent that the flip angle, important as it is, it does not directly show deviation from uniformity. In order to evaluate the homogeneity we employ the ripple in the ROI, that is, the variation of the total magnetic field inside the brain with respect to a reference point, namely:

$$\Delta B_1^+(\underline{r}) = B_1^+(\underline{r}) - B_1^+(\underline{r}_0) \tag{16}$$

If the field in this region is homogeneous we expect the ripple of the field, the quantity above, to vanish. In order to evaluate this parameter we normalize the ripple with respect to the maximum value of the total magnetic field $\underline{B}_1$, normalized ripple (NR):

$$NR(\underline{r}) = \frac{|\Delta B_1^+(\underline{r})|^2}{\left\||B_1^+(\underline{r})|^2\right\|_\infty} \tag{17}$$

Additionally, we will also use another numerical parameter that has been considered to express the homogeneity of the B_1^+ field according to [1]; this parameter is the relative standard deviation (RSD), i.e., the standard deviation divided by the average, namely:

$$RSD = \frac{std\{|B_1^+(\underline{r})|\}}{mean\{|B_1^+(\underline{r})|\}} \tag{18}$$

In order to evaluated polarization uniformity we will employ the following normalized polarization deviation (NPD):

$$NPD(\underline{r}) = \frac{|B_1^-(\underline{r})|^2}{\left\|\underline{B}_1(\underline{r})\right\|_2^2} \tag{19}$$

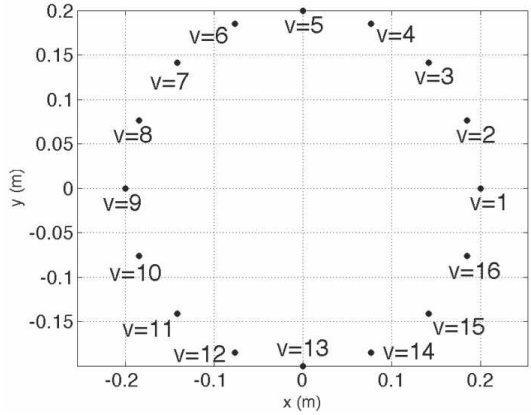

Figure 4. Positions of conductors.

We note that the optimal solution is when $B_1^- = 0$ (pure RH polarization), thus the quantity above (NPD) must vanish to preserve the polarization of the field.

4. NUMERICAL RESULTS

In this section, we will show results of our optimization scheme by considering the parameters described above for the proposed head model.

Before starting to present results, we stress the fact that the proposed optimization method is suitable to operate at any frequency and intensity field. However, we concentrate our analysis on one of the most critical case at high frequency: 300 MHz, which stands for $B_0 = 7\,\mathrm{T}$. The number of excitations (number of unknowns in the optimization procedure) is $Nsrc = 16$ sources. The coefficients $[I]$ at the starting point in (1) and (2) have been selected according to [8]:

$$I_v = I_0 e^{-j\Phi_v} \tag{20}$$

with the phase for the vth conductor set to:

$$\Phi_v = \frac{(v-1)2\pi}{N_{src}} \tag{21}$$

Figure 4 shows the geometry and position for each conductors.

Also, all of our simulations were performed on a PC with Windows Xp 32 bit, 4 GB RAM and Intel 2 Duo processor. With regards to the EM solver, we used a Method of Moments (MoM) with piece-wise constant basis function in 2-D [19]. By using the excitation

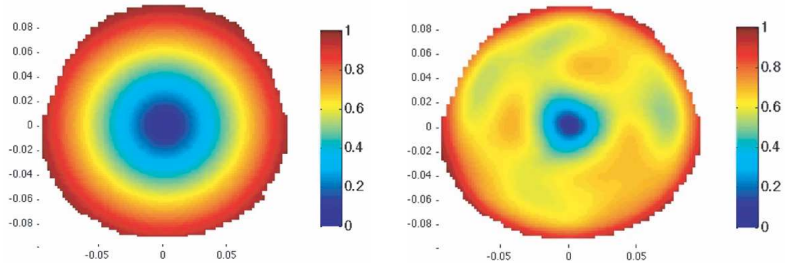

Figure 5. Normalized electric field in unloaded and loaded MRI scanner at f_3. (a) Empty scanner. (b) System coils loaded with the brain model.

coefficients $[I]$ as a point-source excitation [20], we solve the 2-D MoM for Equation (2). Once we compute the electric field, the magnetic induction (1) is obtained through differentiation.

4.1. Application to Realistic Head Model

Here we test the presented approach on the brain model described in Section 3.1; for the sake of conciseness we will consider only the case at frequency $f_3 = 300\,\text{MHz}$ i.e., for a static field $B_0 = 7\,\text{T}$.

First of all, it is instructive to analyze the situation with the conventional choice for the current driving as described in Equations (20), (21). This is reported in Figure 5 showing the electric field obtained before and after inserting the proposed brain model.

As indicated by [8], in the absence of a head inside the scanner system, the electric field produced by the excitations in (20) and (21) varies linearly along the radial direction. When the system coils is loaded with the brain asymmetric model the field loses its symmetry both in radial and azimuthal directions as expected. The field inside the MRI scanner is very inhomogeneous and the polarization of $\underline{B}_1$ field (not shown in the figure) is far from circular.

In order to have an estimate of both the achievable field strength and a goal for realistically improving performances, we employ the field obtained with the usual current driving, i.e., (20) and (21), as a reference in setting the constraints of COPAS optimization; this excitation and the related fields will be indicated as "initial" in the following. For the polarization, we constrain the solution to have an undesired polarization component bounded by 1/2 of that of the initial configuration (at the center of the ROI, where polarization would be

RH in the empty scanner); similarly, using (24) we constraint the optimized field to have a minimum strength no less than 2/3 of the value pertaining to the initial configuration. These specific values (1/2 and 2/3) were suggested by conducting a certain number of tests with different values.

Because of its different functional nature, at a difference with the other constraints, the SAR constraint has been chosen instead in compliance with [6] and [7].

Summarizing, the constraints of COPAS are therefore as follows:

$$SAR(\underline{r}) \leq UBS(\underline{r}) = 3.2\,\mathrm{W/kg} \tag{22}$$

$$|B_1^-(\underline{r})|^2 \leq UBP(\underline{r}) \cdot |B_1^+(\underline{r})|^2 = \frac{1}{2}|B_1^{+^{init}}(\underline{r})|^2 \tag{23}$$

$$B_1^+(\underline{r}_0) \geq B_{1_{desired}}^+ = \frac{2}{3}\left\|Real\{B_1^{+^{init}}(\underline{r})\}\right\|_\infty \tag{24}$$

In the above, the SAR constraint is enforced within the entire scanner volume, while the polarization constraint is enforced only in the ROI.

Before analyzing the results obtained by COPAS with full constraints, we deem it important to analyze the role of polarization constraint. It is intuitive that controlling the ripple of RF field amplitude (i.e., its homogeneity), does not guarantee spatial uniformity in the polarization, but to appreciate that from a quantitative standpoint we conduct a test with the same set-up as for the previous example (23) to (24) but deleting the constraints on polarization (23). As the results in Figure 6 we show that even if the constraints on

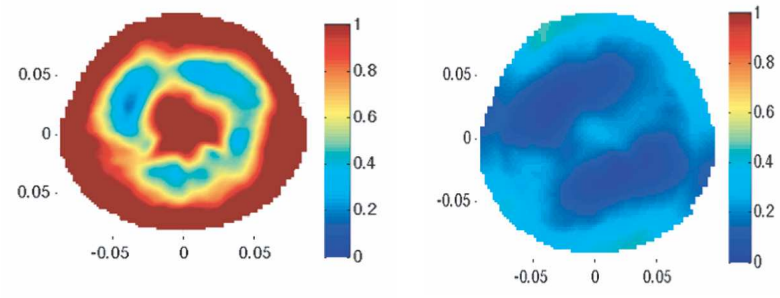

Figure 6. Variation of polarization at f_3. (a) NPD after optimization without constrain on polarization. (b) NPD after optimization with constrain on polarization.

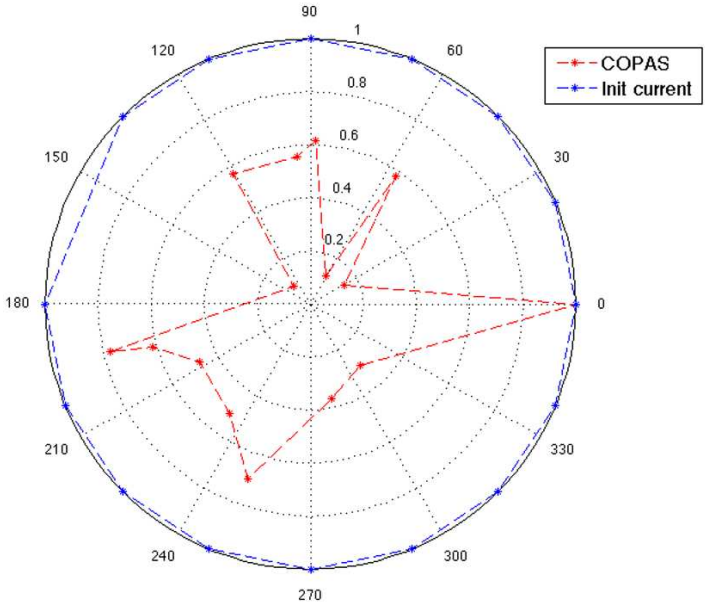

Figure 7. Polar plot for initial and optimized excitation coefficients: normalized amplitude (A), and phase (degree).

ripple, SAR and B_1^+ are completely fulfilled, the polarization is far from uniform (we explicitly omit the ripple and SAR constraints plot).

Finally, before listing the results of COPAS on QI parameters, in Figure 7 we report the distribution of the excitation coefficients (magnitude and phase) for the initial choice in (20), (21) and after the optimization. The results are reported for three different frequencies: f_1, f_3 and f_5. With regards the aforementioned QI parameters we show the SAR in Figure 8, flip-angle in Figure 9, NPD and NR in Figures 10, and 11, respectively.

Also, Figure 12 reports the relative standard deviation for all frequencies listed in Table 2.

As clearly seen from Figure 12, the higher the frequency, the higher the non-homogeneity, and the worse the performance in the absence of optimization. Conversely, at the highest frequency the proposed method shows better performances in fulfilling the constraints and in minimizing the cost function. Also, the percentage variation increases with the B_1^+ frequency (i.e., with B_0 strength) and at the highest selected frequency, f_5, we may encounter a very non homogeneous example. In fact, the relative variation between the RSD before and after COPAS is almost 50%.,

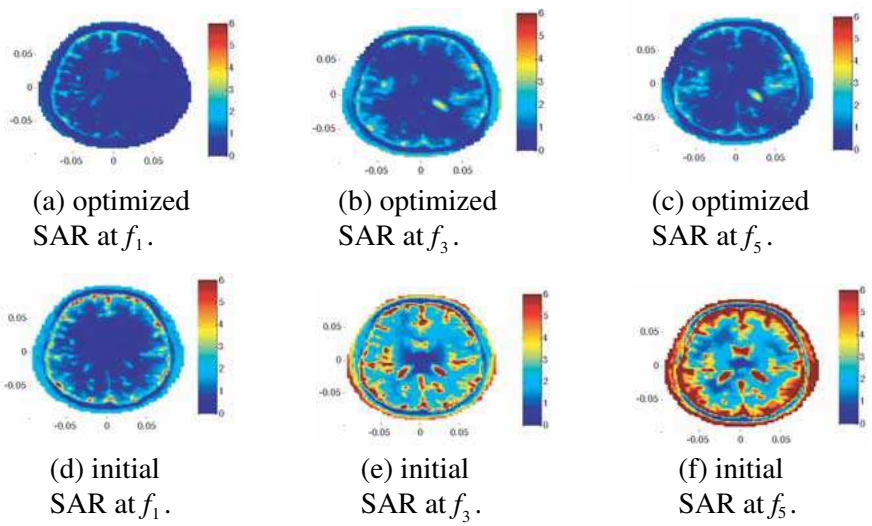

(a) optimized SAR at f_1.

(b) optimized SAR at f_3.

(c) optimized SAR at f_5.

(d) initial SAR at f_1.

(e) initial SAR at f_3.

(f) initial SAR at f_5.

Figure 8. Quality indicators parameters for dielectric head-model: SAR.

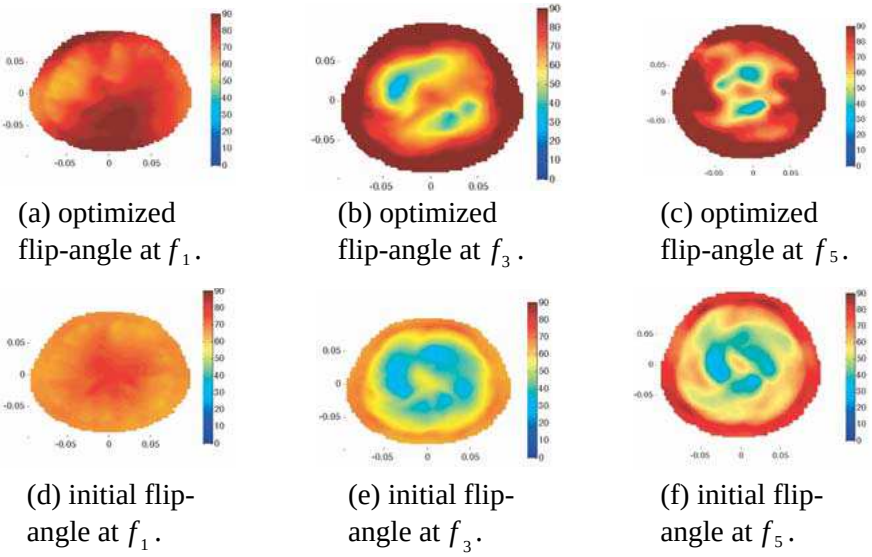

(a) optimized flip-angle at f_1.

(b) optimized flip-angle at f_3.

(c) optimized flip-angle at f_5.

(d) initial flip-angle at f_1.

(e) initial flip-angle at f_3.

(f) initial flip-angle at f_5.

Figure 9. Quality indicators parameters for head-model: flip-angle.

4.2. Verification of Overall Convexity Under Convex Constraints

At a first glance the cost functional (8) is easily recognized as non convex. That is, if X represents the set of all excitation coefficients,

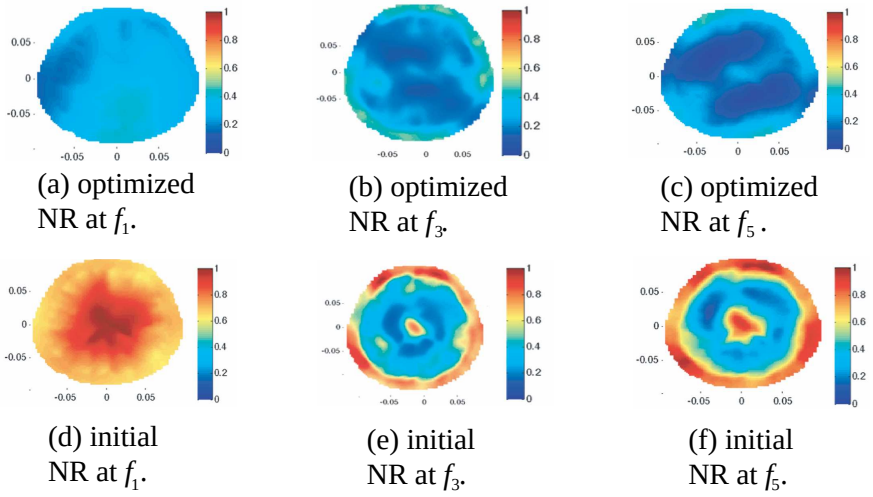

(a) optimized NR at f_1. (b) optimized NR at f_3. (c) optimized NR at f_5.

(d) initial NR at f_1. (e) initial NR at f_3. (f) initial NR at f_5.

Figure 10. Quality indicators parameters for head-model: NR.

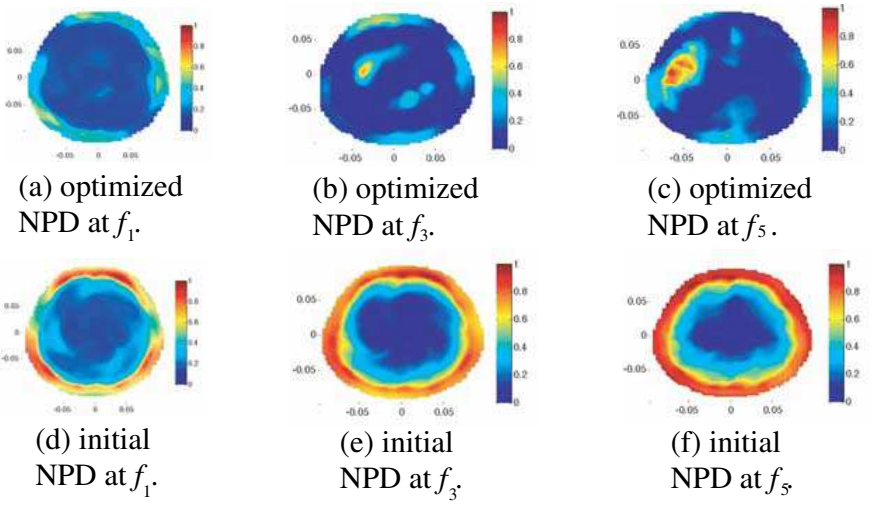

(a) optimized NPD at f_1. (b) optimized NPD at f_3. (c) optimized NPD at f_5.

(d) initial NPD at f_1. (e) initial NPD at f_3. (f) initial NPD at f_5.

Figure 11. Quality indicators parameters for head-model: NPD.

and Y the set of all possible solutions (strength of field, polarization and SAR) then Y is a non convex set. Also, due to the possible presence of relative minima, and due to the non convexity of the set Y, convergence to a local minimum could appear. Thus, we can pick up a false solution of our initial problem. Such points are in general called trap points [21] and they occur when the non convexity of the set Y

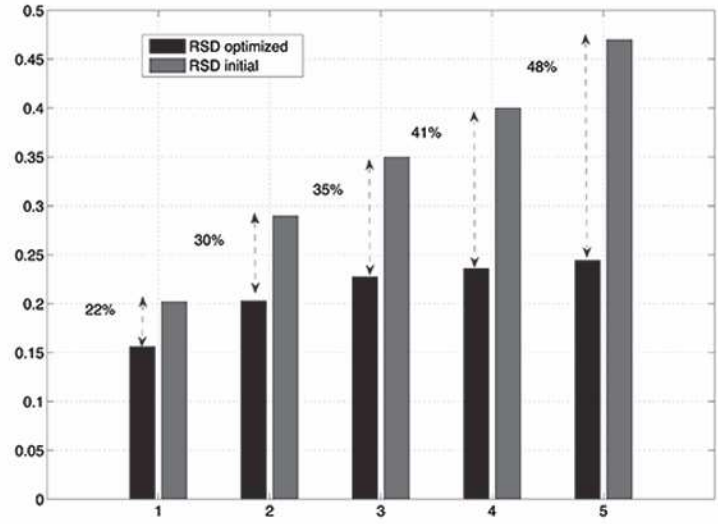

Figure 12. Relative standard deviation for all Larmor frequencies: black bar is the RSD for the initial field, light grey bar is the obtained RSD after COPAS. The percentage is related to the relative variation with respect to the initial RSD.

is involved. The only way to overcome this kind of problem seems, in principle, the adoption of a global optimization algorithm such as a genetic algorithm. Resorting to a global technique allows us to verify that the found minimum for our problem is indeed the global one. In fact, since a rigorous proof of the convexity of the shimming problem under certain constraints is not obtainable, using the GA will provide an empiric confirmation of that.

In the following we report a numerical experiment comparing GA and our optimization procedure for the experiment illustrated in the previous section at f_3. The GA optimization procedure was employed with the parameters listed in Table 5, while COPAS was employed with the parameters selected as in Table 6; Figure 13 depicts the excitation coefficients $[I]$ obtained by using GA and COPAS. We have verified that the fields obtained with excitation coefficients resulting from the global GA optimization fulfill the convex constraints in (9)–(11). For the sake of brevity, we do not report the QI parameters for this solution in view of the fact that there are no significant changes with respect the results obtained with COPAS and depicted in Figures 8–10, and 11.

Moreover, we compute the relative error for magnitude and phase

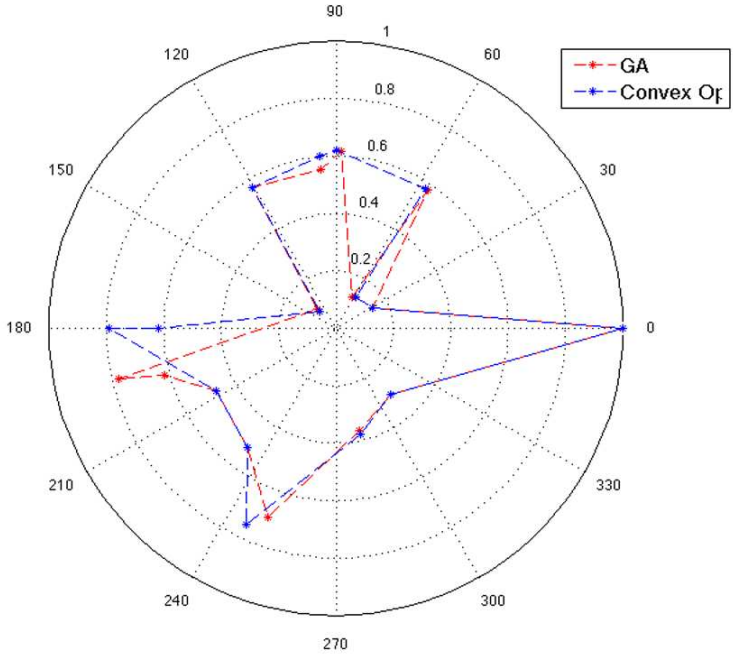

Figure 13. Excitation coefficients for each transmitters at f_3: comparison between GA and COPAS. Polar plot: normalized magnitude (A), and phase (degree).

Table 5. Results using GA with convex constraints.

Number of samples in population	20
Cross over probability	0.8
Mutation probability	0.2
Elite count	2
Number of generations	20
Starting point (X_0)	randomly selected
Selection function	stochastic uniform
Stopping criteria (tolerance on fitness)	$2e-2$
Final function value	0.0104252
Number of function callings	9507
Total time	600 sec

between GA and our method as followings:

$$\epsilon_{|I|} = \frac{\left\| |I_{GA}| - |I_{conv}| \right\|_2^2}{\left\| |I_{conv}| \right\|_2^2} = 0.023 \tag{25}$$

Table 6. Results using COPAS.

Iteration numbers	15
Stopping criteria (tolerance on fitness)	$2e-2$
Final function value	0.0089
Number of function callings	165
Total time	150 sec

$$\epsilon_{\angle I} = \frac{\left\| \angle I_{GA} - \angle I_{conv} \right\|_2^2}{\left\| \angle I_{conv} \right\|_2^2} = 0.032 \tag{26}$$

It is apparent from the above that, while requiring a rather different number of iterations, both global GA and convex COPAS algorithms converged to the same result; this can be explained only resorting to a convexity of the problem in the set Y (i.e., of the functional subject to the examined constrained). Even if the shimming problem is non convex in general, the constraints on SAR, ripple, and polarization tends to delete the non convex nature of the problem. We can now classify the shimming problem as convex under certain constraints. A similar behavior was observed in many practical problems ([22, 23] and this allows us to use any local minimization algorithm to get a global solution.

5. CONCLUSIONS AND FUTURE WORK

A novel approach for shimming the RF field (B_1^+) in MRI has been proposed that employs an optimization procedure with convex constraints (COPAS). The convexity of the presented approach is crucial: it ensures to achieve the global minimum of the problem. Such a formulation allowed us to have an accurate, repeatable, and optimal solution of the shimming problem.

Also, by using this procedure we were able to reduce the SAR and control the uniformity and polarization of the $\underline{B}_1$-field. The role of polarization has been studied and tested on an application instance confirming the importance of such parameter. Contrary to other shimming procedures, controlling the polarization of the field allows to reduce the polarization change for the total RF $\underline{B}_1$-field. The proposed method has been tested also with medium and high MRI (static) field values. We show that in virtue of the constraints, a convex optimization procedure applied to a non convex functional produces a solution that is a global optimum, as verified using genetic algorithm

(GA) to check the obtained solution. We have shown results relative to brain imaging MRI in 2-D. Future works will involve application of COPAS on 3-D problem. In this case, special care must be devoted to develop and design the birdcage in 3-D for high-field MRI. As outlined in [24], producing a magnetic field $\underline{B}_1$ with a desired strength inside the birdcage is far to be trivial and different configurations have been proposed for both birdcage and TEM coil. The development of a 3-D model for the birdcage is under our investigation, while the proposed optimization scheme needs not be changed.

REFERENCES

1. Mao, W., M. B. Simth, and C. M. Collins, "Exploring the limits of rf shimming for high-field mri of the human head," *Magn. Res. in Med.*, Vol. 56, 918–922, 2006.
2. Ibrahim, T. S., R. Lee, B. A. Baertlein, and P.-M. L. Robitaille, "B_1 field homogeneity and SAR calculations for the birdcage coil," *Phys. Med. Biol.*, Vol. 46, 609–619, 2001.
3. Van Den Bergen, B., C. A. T. Van Den Berg, L. W. Bartels, and J. J. W. Lagendijk, "7 T body MRI: B_1 shimming with simultaneous SAR reduction," *Phys. Med. Biol.*, Vol. 57, 5429–5441, 2007.
4. Ibrahim, T. S., Y.-K. Hueb, and L. Tangc, "Understanding and manipulating RF fields at high field MRI," *NMR Med.*, Vol. 22, 927–936, 2009.
5. Haacke, E. M., R. W. Brown, M. R. Thompson, and R. Venkatesan, *Magnetic Resonance Imaging: Physical Principles and Sequence Design*, Wiley-Liss, 1999.
6. Zaremba, L., "FDA guidelines for magnetic resonance equipment safety," *Proc. American Ass. of Phys. in Med.*, 2002.
7. ICNIRP, "Guidelines for limiting exposure to time-varing electric, magnetic and electromagnetic fields (up to 300 GHz)," *Health Phys.*, 1998.
8. Jin, J., *Electromagnetic Analysis and Design in Mgnetic Resonance Imaging*, CRC Press, 1997.
9. Isernia, T. and G. Panariello, "Optimal focusing of scalar fields subject to arbitrary upper bounds," *Electronics Letters*, Vol. 34, 162–164, 1998.
10. Isernia, T., O. M. Bucci, and N. Fiorentino, "Shaped beam antenna synthesis problems: Feasibility criteria and new strategies," *Journal of Electromagnetic Waves and Applications*, Vol. 12, No. 1, 103–138, 1998.

11. Isernia, T., F. Soldovieri, G. Leone, and R. Pierri, "Role of support information and zero locations in phase retrieval by a quadratic approach," *Journal of the Optical Society of America A: Optics, Image Science, and Vision*, Vol. 16, 1845–1856, 1999.
12. Dennis, Jr., J. E., "Nonlinear least-squares," *State of the Art in Numerical Analysis*, 269–312, Ed., D. Jacobs, Academic Press, 1997.
13. Kwan, R. K. S., A. C. Evans, and G. B. Pike, "MRI simulation-based evaluation of image-processing and classification methods," *IEEE Trans. on Med. Im.*, Vol. 18, 1085–1097, 1998.
14. http://mouldy.bic.mni.mcgill.ca/brainweb/.
15. Gabriel, C., S. Gabriel, and E. Corthout, "The dielectric properties of biological tissues: I. Literature survey," *Phys. Med. Biol.*, Vol. 41, 2231–2249, 1996.
16. Gabriel, S., R. W. Lau, and C. Gabriel, "The dielectric properties of biological tissues: II. Measurements in the frequency range 10 Hz to 20 GHz," *Phys. Med. Biol.*, Vol. 41, 2251–2269, 1996.
17. Gabriel, S., R. W. Lau, and C. Gabriel, "The dielectric properties of biological tissues: III. Parametric models for the dielectric spectrum of tissues," *Phys. Med. Biol.*, Vol. 41, 2271–2293, 1996.
18. Glanze, W. G., K. Anderson, and T. Myers, *Mosby's Medical Dictionary*, Elsevier, 2009.
19. Peterson, P. and R. Mittra, *Computational Methods for Electromagnetics*, 1st edition, IEEE Press, 1997.
20. Balanis, C., *Advanced Engineering Electromagnetics*, Solution Manual Edition, Wiley, 1989.
21. Nocedal, J. and J. Wright, *Numerical Optimization*, 2nd edition, Springer, 1996.
22. Bucci, O. M., M. Cardace, L. Crocco, and T. Isernia, "Degree of nonlinearity and new solution procedure in scalar two-dimensional inverse scattering problems," *J. Opt. Soc. Am.*, Vol. 18, 1832–1843, 2001.
23. Bucci, O. M., M. D'Urso, and T. Isernia, "Optimal synthesis of difference patterns subject to arbitrary sidelobe bounds by using arbitrary array antennas," *IEEE Proceedings in Microwaves, Antennas and Propagation*, 129–137, 2005.
24. Wu, B., C. Wang, D. A. C. Kelley, D. Xu, D. B. Vigneron, S. J. Nelson, and X. Zhang, "Shielded microstrip array for 7 T human MR imaging," *IEEE Trans. on Med. Im.*, Vol. 29, 179–185, 2010.